Grid-Forming Services From Hydrogen Electrolyzers

Saman Dadjo Tavakoli, Mehdi Ghazavi Dozein, *Senior Member, IEEE*, Vinícius A. Lacerda, Marc Cheah Mañe, *Member, IEEE*, Eduardo Prieto-Araujo, *Senior Member, IEEE*, Pierluigi Mancarella, *Fellow, IEEE*, and Oriol Gomis-Bellmunt, *Fellow, IEEE*

Abstract—Hydrogen electrloyzers are power-to-gas storage devices that can facilitate large-scale integration of intermittent renewable sources into the future power systems. Due to their fast response and capability to operate in different loading conditions, they can be used as responsive loads providing support to AC grid during transients. This paper suggests taking one step further and using hydrogen electrolyzers to provide grid-forming services to the grid. As a result, the electrolyzer's role is elevated from supporting the grid (responsive load) to actively participating in forming voltage and frequency of the grid. The grid-forming capability of electrolyzer is linked to its hydrogen production constraints, which can potentially pose limitations on the grid-forming services. Besides the grid-forming mode, two additional operating modes, i.e., DC voltage mode and constant power mode, are proposed to ensure a safe operation of the electrolyzer in case of adversary interaction between grid-forming operation and hydrogen production constraints. This paper also studies the impacts of grid-forming services on the electrolyzer's physical features such as hydrogen stack temperature and efficiency. Comprehensive simulations are conducted on a low-inertia test network whose topology is inspired by a portion of the transmission grid in South Australia to confirm the effectiveness of the proposed concept under various operational conditions of the electrolyzer and upstream AC grid. Moreover, the practical feasibility of the proposed control system is experimentally validated by conducting hardware-in-the-loop tests.

Index Terms—Hydrogen electrolyzer, Storage, Responsive load, Grid-forming load.

I. INTRODUCTION

Hydrogen electrolyzers (HE) are electrochemical devices used to split water molecules into hydrogen (H_2) and oxygen (O_2) by passage of a DC current. They provide power-to-gas energy storage solution which creates opportunities to leverage intermittent renewable generations [1]. Major HE technologies are polymer electrolyte membrane (PEM), alkaline with liquid or solid electrolyte, and recently solid oxide electrolyzer. PEM electrolyzers are manufactured from small sizes (several kilowatts) up to large, utility-scale systems (multi-megawatt plants) [2]. They can respond to changes in their power set-points in sub-second time frame and operate at a wide range of loading conditions [3]. In [2], it is experimentally identified that a PEM electrolyzer takes only few hundred milliseconds to change its hydrogen production rate in response to step changes in the power set-point.

Hydrogen production in an electrolyzer is directly proportional to its power consumption. The produced hydrogen is typically stored in a large H_2 tank, from which the hydrogen is consumed by a downstream process [4]. Such H_2 tank acts as a buffer, so that hydrogen can be produced in a different rate than it is consumed as long as the hydrogen content in the tank is enough to supply the downstream hydrogen demand

continuously. This creates an opportunity for HE to operate in different power set-points (different loading conditions) without affecting the downstream hydrogen consumption [5], [6]. Such flexibility in power consumption, along with the ability to respond to the changes in sub-second time frame, makes an electrolyzer as a potential candidate to be used as a responsive load which supports AC grid dynamics during fast transients.

Although several studies have already investigated the techno-economic aspects of integrating HE as a power-to-gas storage in power systems for maximizing the benefits from the intermittent renewable energy sources [7]–[10], only few studies have been conducted to identify the full potential of HE as a responsive load. In [2], [11]–[13], it has been shown that a HE can effectively operate as a responsive load to reduce frequency deviations during grid disturbances. In these studies, the HE plant is interconnected to the AC grid via voltage-source converter (VSC) that operates in grid-following (GFL) mode. In such operation mode, the active power set-point of the VSC defines the power consumption of the HE. To make HE operate as a responsive load , an active power-frequency characteristic is added to the power control loop of the HE VSC so that the HE power consumption varies as a response to frequency variations. However, these studies either fully or partially disregard the dynamics of the HE plant; in particular, the operational constraints related to the hydrogen production process are not linked to the control system of HE VSC. In [14], the control system of HE VSC is designed based on GFL operation and the hydrogen production constraints are considered. It is discussed that the hydrogen content in the tank may pose limitations on the active power set-point of the HE VSC, and eventually its capability in frequency response provision.

Recently, it has been shown that dispatchable loads with demand flexibility can provide grid-forming services to the AC grid [15]. In this concept, the role of loads in power system is elevated from providing only frequency support to actually participating in forming the voltage and frequency of the grid. In fact, the power balance in the grid can be mostly achieved through load demand variations rather than changes on the generation side. To that aim, a grid-forming load regulates frequency and AC voltage of the grid by, respectively, regulating its power consumption and reactive power exchange. It should be noted that such concept is only applicable to the loads that are connected to AC grid via a VSC, so active and reactive power can be regulated independently at the point of connection. Several studies have considered grid-forming functionality for hydrogen electrolyzer, most often with the combination of a fuel cell unit [16], [17]. The hybrid

electrolyzer-fuel cell unit can operate in grid-forming mode and depending on the loading condition in the AC grid, the hybrid unit can either inject power to or absorb power from the AC grid.

This paper explores the feasibility of implementing the grid-forming (GFM) functionality in the HE VSC with the consideration of hydrogen production constraints. The advantages are twofold: (i) the function of HE in the power system will change from responsive load (GFL control) to grid-forming load (GFM control); hence, the HE actively participates in forming voltage and frequency of the AC grid instead of only supporting it, (ii) the tandem operation of HE with a nearby renewable source enables islanded operation in case of contingency in the AC grid. The HE operation in GFM mode may interact with the constraints in hydrogen production, which can negatively affect HE grid-forming capability. Under this condition, two additional operating modes are proposed: DC voltage mode which is activated if the hydrogen plant is shut down due to an internal failure in the electrolyzer or the hydrogen tank is full, and constant power mode which is brought to operation in case the hydrogen content in the tank is critically low and the downstream hydrogen demand may not be fulfilled. A PEM HE with the proposed control system is integrated into a low-inertia test network whose topology is inspired by a portion of the transmission grid in South Australia. Matlab simulations are conducted on such system to compare the dynamic performances of these operation modes during disturbances in the grid, confirming the ability of HE to safely switch among different operation modes under abnormal conditions in the hydrogen production process and AC grid. We also investigate the impact of grid-forming services from hydrogen electrolyzer on its physical features such as temperature and efficiency. Finally, the HE is compared with a battery storage system in terms of their capabilities in providing grid-forming services. The contributions of this study can be summarized as follows:

- Proposing a dynamic modelling framework for hydrogen electrolyzers equipped with three operation modes (i.e., grid-forming mode, DC voltage mode, and constant power mode),
- Highlighting possible interactions between HE grid-forming services and the operational constraints in hydrogen production, as well as proposing the corresponding solutions,
- Studying the impacts of HE grid-forming operation on the physical features of HE such as temperature and efficiency.

II. FUNDAMENTALS OF HE DYNAMIC MODELING

In this section, the basic operation of a PEM HE is outlined, and its dynamical model is developed. The constraints related to the hydrogen production process are also discussed through its fundamental equations.

A. Basic HE Operation Principles

Referring to [1], [4], a simplified process flow diagram of a PEM HE is shown at the bottom of Fig. 1. The deionized water is supplied to a water tank (marked by ①) from which it is fed into the PEM stack (anode side) via a water pump. The applied DC voltage at the stack, V_h^{dc}, causes water split to hydrogen and oxygen. This process draws a DC current, I_h^{dc}. The oxygen is then passed through a gas-water separator (③) in which oxygen is separated from water. The remained water is removed at the bottom and returned to the PEM stack via a circulation pump, while the oxygen is released from the top. On the cathode side, the produced hydrogen is passed through a gas separator (⑥) to eliminate the remaining water in the gas. After cooling down in a heat exchanger, hydrogen is passed through the gas condensate and de-oxygenation (⑦ and ⑧, respectively). Then, it is fed into a gas dryer (⑩) through a compressor. Finally, the produced hydrogen is stored in the tank (⑪) which acts as a buffer between hydrogen production and consumption.

B. Efficiency and Temperature of PEM stack

The voltage-current characteristic of a single PEM cell is shown in Fig. 2, which illustrates a direct relationship between cell's voltage and current: a higher current passing through the cell causes a slight increase in the cell's voltage. With regard to the cell's efficiency, a higher current density leads to the greater losses inside the cell, and thus the efficiency is reduced. On the contrary, if a PEM cell is allowed to operate in a higher temperature, it will have higher efficiency for the same current density. However, higher operating temperature has a negative impact on ageing and longevity of the cell. Hence, the optimal temperature is commonly decided to find a balance between efficiency and the service life [18].

C. HE Dynamical Model

There are two major methods for building the dynamical model of an electrolyzer: (i) using the exact mathematics that represent the chemical reaction in the cells and the dynamics of major ancillary equipment, such as pumps, compressors, heaters, etc., to derive the HE model [19]–[21]; and (ii) experimentally identifying the electrolyzer model based on its DC terminal characteristics [2], [22]. The former method, of course, can obtain model with a very high accuracy, provided that all details and parameters of the HE system is available. Then, the equations related to the chemical reactions in the cathode, anode, and the membrane are derived and coupled with those of water pumps, cooling fans, storage tanks, etc., to arrive at the final model. However, a disadvantage of such complex approach, particularly in a multi-vendor HE project where several companies deal with various parts of the project, is that the design parameters of the electrolyzer are often proprietary information which companies wish to keep confidential.

In the latter modeling method, on the other hand, the HE's dynamic behaviour is analysed only based on its DC voltage-current characteristics at the connection point (V_h^{dc}-I_h^{dc} shown in Fig. 1), which is more suitable for power system studies. In this method, the power reference of the HE is varied between a very low power to the rated power and the result DC current and voltage are plotted [2]. From these plots, a general transfer
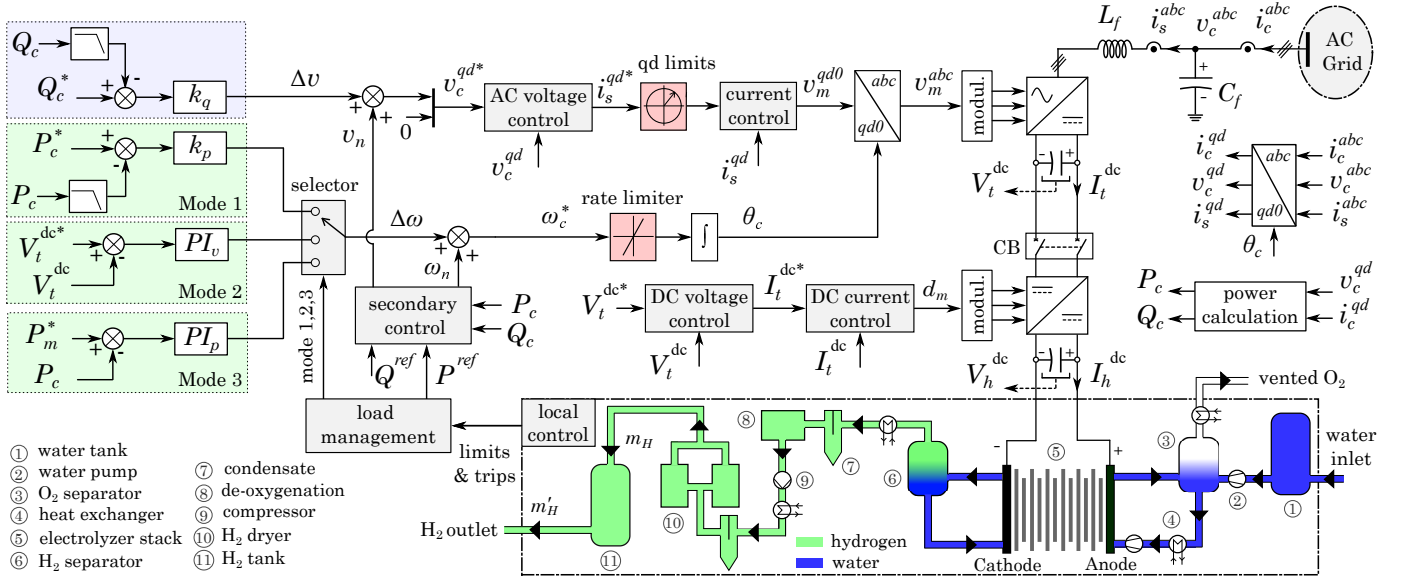
Fig. 1. Overall system structure of a PEM hydrogen electrolyzer

① water tank
② water pump
③ O₂ separator
④ heat exchanger
⑤ electrolyzer stack
⑥ H₂ separator
⑦ condensate
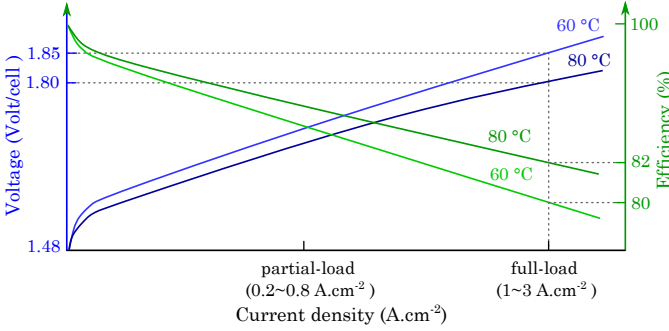⑧ de-oxygenation
⑨ compressor
⑩ H₂ dryer
⑪ H₂ tank

Fig. 2. Voltage-current and efficiency of a PEM cell [18]

function which relates DC current to the DC voltage at the terminal of the HE is estimated. Such modelling technique is developed in [23] and adopted in this study.

Referring to [23], the dynamics of the PEM HE can be formulated into a second-order transfer function:

$$H(s) = \frac{I_h^{\text{dc}}}{V_h^{\text{dc}}} = \frac{p_1 p_2\,(s - z)}{(s - p_1)(s - p_2)} \tag{1}$$

where V_h^{dc} and I_h^{dc} are DC voltage and current at the HE terminal, respectively. The poles, p_1 and p_2, are located on the left half plane (LHP) and calculated based on the rise time, t_r, and settling time, t_s, measured from the HE transient response,

$$\ln\Big(\frac{p_2}{p_1 - p_2} + \frac{p_1}{p_2 - p_1} e^{\frac{p_2}{p_1}}\Big) - p_1 t_s = \ln(-y_{ss}) \tag{2}$$

$$\ln\Big(\frac{p_2}{p_1 - p_2} + \frac{p_1}{p_2 - p_1} e^{\frac{p_2}{p_1}}\Big) - p_1 t_r = \ln(-y_r) \tag{3}$$

where y_{ss}=0.05, corresponding to the response's steady-state error at the settling time, commonly 5%, and y_r=0.5, which is related to 50% of response at the rise time. Once p_1 and p_2 are calculated, the zero, z, is selected to be within the LHP region given by

$$p_1 + p_2\ < z \le\ p_1 \tag{4}$$

In fact, only t_r and t_s from the experiment are needed to

calculate $H(s)$. Such transfer function represents an equivalent electrical circuit in which a DC voltage source and RC elements are connected in series as illustrated in Fig. 3. The DC voltage source, V_{rev}, represents the reverse voltage, i.e., the minimum voltage that allows the current flow through the PEM stack,

$$V_{rev} = V_{rev0} + \frac{R\,T}{2F} \ln\Big(\frac{P}{P_0}\Big) \tag{5}$$

where, P and T are stack pressure and temperature, respectively; V_{rev0} and P_0 are reference voltage and pressure; R is the ideal gas constant expressed in 1 atm K⁻¹ mol⁻¹, and F is the Faraday constant. The passive electrical components are calculated based on the poles and zero of $H(s)$ as

$$C_{op} = \frac{-p_1 p_2}{z(z^2 - z(p_1 + p_2) + p_1 p_2)} \tag{6}$$

$$R_m = \frac{z^2 - z(p_1 + p_2) + p_1 p_2}{p_1 p_2} \tag{7}$$

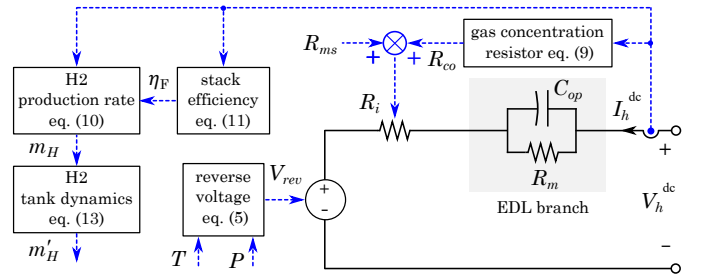$$R_i = \frac{z(p_1 + p_2 - z)}{p_1 p_2} \tag{8}$$

Fig. 3. Equivalent model of a PEM hydrogen electrolyzer

The parallel connection of C_{op} and R_m accounts for the electrical double layer (EDL) phenomenon, which is related to the non-uniform distribution of negative and positive charges at the electrode-electrolyte interface. The EDL phenomenon creates an energy barrier against the flow of electrons when

there is a need for sudden current change, which leads to a response delay. Moreover, this phenomenon causes a transport loss as modelled by R_m.

The internal resistance, R_i, is the sum of two resistances: (i) resistance of the stack material, R_{ms}, and (ii) the resistance related to the concentration of hydrogen and oxygen on the electrode surface, R_{co}, which acts as a barrier to the flow of electron to reach the electrodes. R_{co} is a non-linear function of the HE's current,

$$R_{co} = \beta_1 \ln \left(\frac{\beta_2}{A} I_h^{\text{dc}} + 1 \right) \tag{9}$$

where the constant coefficients, β_1 and β_2, are obtained from measurements, and A is the electrode surface. Please see [23] for further details.

D. HE Operational Constraints

The PEM HE is allowed to operate within a power consumption range, resulting in variations in its input DC current, I_h^{dc}. Such demand flexibility comes from the ability of HE to produce hydrogen in varying rates. Hydrogen production rate, m_H in Moles/s, is a function of I_h^{dc}, as

$$m_H = \eta_F \frac{N_s}{2F} I_h^{\text{dc}} \tag{10}$$

where F is the Faraday constant and N_s is the number of cells per stack. The Faraday efficiency, η_F, is the ratio between the actual and theoretical maximum amount of hydrogen as produced by the HE. It is also a non-linear function of I_h^{dc},

$$\eta_F = \alpha_1 \exp \left(\frac{\alpha_2}{I_h^{\text{dc}}} + \frac{\alpha_3}{(I_h^{\text{dc}})^2} \right) \tag{11}$$

where α_1, α_2, and α_3 are constant coefficients obtained from experiments [23], [24]. As given by (11), the hydrogen production efficiency is reversely related to the current, i.e., efficiency drops for higher currents (also see Fig. 2).

As illustrated in Fig. 1, the produced hydrogen, with the rate given by m_H, is transferred to a storage (H$_2$ tank ⑪). The outlet of the storage supplies the hydrogen demand which is given as hydrogen consumption rate, m'_H. Such configuration provides a buffer zone for hydrogen; hence, depending on the size of the storage, there can be a mismatch between hydrogen production and consumption rates, which provides a great source of flexibility for the power system. In fact, the PEM HE can vary its power consumption to produce hydrogen in a varying rate as long as the hydrogen content in the tank (buffer) is within the range given by

$$V_H^{\text{min}} \le V_H(t) \le V_H^{\text{max}} \tag{12}$$

where V_H^{min} is the minimum hydrogen content in the H$_2$ tank that guarantees a steady hydrogen supply for the downstream process (hydrogen consumption), and V_H^{max} is the maximum capacity of the H$_2$ tank. So long as V_H is within the limits, the HE can be regarded as a fully flexible load capable of providing GFM services to the grid, i.e., varying its active power consumption depending on the grid's frequency deviation.

The capacity constraint on the H$_2$ storage given by (12) can be expressed in terms of the stack's current as follows:

assuming a disturbance occurs in the grid at $t = t_0$, the HE adjusts its power consumption automatically (based on the GFM control) to respond to such event. The change in the power consumption leads to a change in hydrogen production rate (m_H), affecting the hydrogen content in the tank over this period of time,

$$V_H(t) = V_H^0 + \int_{t_0}^t m_H(t)\, dt \; - \int_{t_0}^t m'_H(t)\, dt \tag{13}$$

where V_H^0 is the initial content of hydrogen in the tank at $t = t_0$. A time horizon of t_h is considered. If it is small enough, the hydrogen consumption rate, $m'_H(t)$, can be assumed to be constant due to the slow dynamics of the downstream hydrogen consumption. With such assumption, (13) can be simplified and combined with (12) to arrive at:

$$V_H^{\text{min}} - V_H^0 + m'_H(t_h - t_0) \le \int_{t_0}^{t_h} m_H(t)\, dt \; \le \\ V_H^{\text{max}} - V_H^0 + m'_H(t_h - t_0) \tag{14}$$

Referring to (10), and calculating the Taylor approximation of (11), the integration of $m_H(t)$ in (14) can be expressed as:

$$\int_{t_0}^{t_h} m_H(t)\, dt \; \approx \\ \frac{N_s \alpha_1}{2F} \left(\int_{t_0}^{t_h} \left(I_h^{\text{dc}}(t) + \frac{\alpha_3}{I_h^{\text{dc}}(t)} \right) dt \; + \alpha_2(t_h - t_0) \right) \tag{15}$$

In large-scale HE applications, DC current I_h^{dc} is significantly larger than α_3 in (15). Hence, the second term (α_3/I_h^{dc}) under integral is much smaller than the first term (I_h^{dc}), which can be ignored. Replacing (15) into (14), a constraint on hydrogen production with respect to stack's current is defined as:

$$S^{\text{min}} \le \int_{t_0}^{t_h} I_h^{\text{dc}}(t)\, dt \; \le S^{\text{max}} \tag{16}$$

where the maximum and minimum are calculated as,

$$S^{\text{min}} = \frac{2F}{N_s \alpha_1} (V_H^{\text{min}} - V_H^0 + m'_H(t_h - t_0)) - \alpha_2(t_h - t_0)$$

$$S^{\text{max}} = \frac{2F}{N_s \alpha_1} (V_H^{\text{max}} - V_H^0 + m'_H(t_h - t_0)) - \alpha_2(t_h - t_0)$$

During the normal operation of HE, when there is no internal fault, S^{min} and S^{max} can be regarded as the upper and lower limits for the flexible operation of the HE, i.e., if the constraint (16) holds, the electrolyzer can operate based on the GFM law and flexibly varies its active power depending on the frequency conditions in the grid. Variations in the active power lead to the changes in the DC current of HE, I_h^{dc}, which directly impacts the efficiency (η_F as given by (11)) and temperature of the PEM stack. As explained earlier (please also see Fig. 2), higher I_h^{dc} causes higher losses in the stack (lower efficiency). The losses appear as heat in the stack which is calculated as

$$q_h = I_h^{\text{dc}} V_h^{\text{dc}} (1 - \eta_F) \tag{17}$$

where q_h is the generated heat (in Watts) in the stack. Depending on the stack's material and dimension, such generated heat can change the operation temperature of the stack [19].

III. PROPOSED HE CONTROL: OPERATION MODES AND LIMITATIONS

In this section, a control system for the PEM HE is suggested. It has three control modes, each activated depending on the HE operational constraints in hydrogen production.

A. Control Principles

The proposed control structure for the PEM HE is shown in Fig. 1. It consists of the HE VSC's cascaded control with the proposed three operation modes and the DC-link voltage control of a DC-DC converter. The following major control blocks are used in this control scheme:

- *Current control*: it regulates the HE VSC's output current, i_s^{qd}, at the references provided by the outer AC voltage control. The output of the current control loops, v_m^{qd0}, is transformed to the abc-frame via angle θ_c to build the modulation signal. The time response of the current control is commonly a few milliseconds.
- *AC voltage control*: the outer AC voltage control regulates HE VSC's output voltage, v_c^{qd}, at the references which are generated by the reactive power droop. The time response of the voltage control is at least ten times slower than that of the current control.
- *Reactive power droop*: a droop gain, k_q, is used to generate voltage reference in q-axis, v_c^{q*}, from the reactive power. The voltage reference in d-axis is set to zero. The peak of the base AC voltage is given by v_n, which comes from a secondary controller. The reactive power-voltage droop is expressed by

$$v_c^{q*} = k_q \ (Q_c^* - G_q(s) \ Q_c) + v_n \qquad (18)$$

where $G_q(s)=1/(\tau_q s + 1)$ is a low-pass filter with a time constant of τ_q used to regulates the speed of voltage support.
- *DC voltage control*: depending on the control mode of the HE, the DC-link voltage, V_t^{dc}, is tightly regulated at the nominal value via either (i) DC voltage control loops of the DC-DC converter (operation Modes 1 and 3) or (ii) the DC voltage control of the HE VSC (operation Mode 2). At any given time, only one of these two controls is activated. The mentioned operating modes are discussed in details in the next section.
- *Secondary control*: it defines the steady-state operation of the electrolyzer as given by the active and reactive power references, P^{ref} and Q^{ref}, respectively. The secondary controller uses a very slow PI controller [25], commonly with a response time of few minutes, so it does not affect the primary response from the electrolyzer. If the secondary controller is activated, the power consumption of the electrolyzer always goes back to P^{ref} with a very slow time constant. The load management control division provides active power reference for the secondary control.
- *Load management*: located between HE local control and the HE VSC's secondary control, it ensures that the operation of HE VSC does not violate the limitations related to the hydrogen production process. More specifically, it monitors whether the constraint given by (16) holds or not. Based on the outcome, one of the HE VSC's operation modes

(Modes 1, 2, 3) are selected, which are explained in the next section.
- *HE local control*: this is the manufacturer's controller that locally regulates HE plant. It receives local signals, such as H_2 tank level, tank pressure, stack temperature, H_2 production and consumption flow rates, etc., and generates valve's positions, pumps and fans' speeds, etc. In case of any failures during HE operation, an alarm/trip signal is sent to the load management control block.

B. Modes of Operation

Referring to (16), for every time horizon of t_h, the upper and lower limits of hydrogen production process, S^{max} and S^{min} given by (16), respectively, are calculated. If the integration of $I_h^{dc}(t)$ violates either of the limits during this time horizon, the HE VSC's operation mode will change to ensure a safe operation of the electrolyzer. Three operation modes are proposed for the HE VSC, and the load management control block is in charge of choosing the appropriate one. As illustrated in Fig. 1, all three modes are related to the specific ways of generating frequency deviation needed to determine the power consumption of the HE.

1) Mode 1: this is the grid-forming operation mode of the HE VSC, and the HE plant can be regarded as a grid-forming load. The integration of $I_h^{dc}(t)$ is within the constraint given by (16), and no trip/alarm signals are sent from HE local control to the load management block. The DC-link voltage is regulated by the control loops of the DC-DC converter, and the HE VSC is allowed to operate fully according to the GFM law, i.e., the power consumption of HE is flexibly varied according to the variations in the grid's frequency. A droop gain, k_p, is used to link HE VSC's active power to the frequency deviation. The output frequency deviation is added to the based frequency, ω_n, to build the operating frequency of the converter, ω_c^*. A low-pass filter is placed on the feedback from the measured active power to emulate virtual inertia in the control system. The droop equation is given as

$$\omega_c^* = k_p \ (P_c^* - G_p(s) \ P_c) + \omega_n \qquad (19)$$

where $G_p(s)=1/(\tau_p s+1)$ is a low-pass filter with time constant of τ_p.

2) Mode 2: in this mode, the hydrogen production process is experiencing an abnormal condition. A possibility is that the H_2 tank is nearly full and it cannot store any further hydrogen. Hence, the integration of $I_h^{dc}(t)$ violates S^{max} in (16), and therefore the operation Mode 2 is activated. Another possibility is that a trip related to a component failure in the hydrogen production process, such as a pump, compressor, dryer, etc., or abnormal stack temperature and pressure, is triggered. In such conditions, the HE needs to be shut down and remained offline for certain duration until it is ready for normal operation again. During this period, the HE and the DC-DC converter are disconnected by the circuit breaker (CB) shown in Fig. 1. As the DC-DC converter is no longer available for DC-link voltage control, the HE VSC's control fulfils such control objective by the activation of Mode 2. In this mode, a dedicated PI controller, PI_v, ensures a tight DC-link voltage

regulation. Although the HE VSC could be disconnected during this period too, it is suggested keeping it connected to the grid to provide AC voltage regulation services. A limited amount of active power is absorbed from the grid only to charge the DC-link capacitor and cover converter's losses. The operation Mode 2 cannot offer grid-forming services as in Mode 1 due to its limited ability in varying its active power consumption.

3) Mode 3: when the hydrogen content in the tank is critically low, and the downstream hydrogen demand may not be fulfilled given the current hydrogen production rate, the HE VSC can switch to Mode 3 to operate in constant power mode, and steadily absorbs high power from the grid. In this operation mode, the HE plant does not flexibly adjust its power consumption to provide frequency support to the grid. The operation Mode 3 is activated automatically in case the integration of $I_h^{dc}(t)$ violates S^{min} in (16). In this operation mode, a PI controller, PI_p, is used to track the active power reference given by P_m^*.

In summary, if the internal operation of the HE plant is normal and no constraints are violated, the HE is allowed to operate in Mode 1 (grid-forming mode). However, if the load management block detects any abnormal condition in the HE plant, it automatically switches to either operation Mode 2 or 3 (non grid-forming modes) depending on the type of the abnormality. However, such mode changing can have a negative impact on the grid's frequency as it causes a change in the power consumption of the electrolyzer. Hence, if it is requested by the grid operator, a frequency condition criterion can be added to the mode selection logic in the load management block to only switch modes during normal grid's frequency conditions (i.e., the grid frequency is experiencing no major over or under frequency events).

C. Control Tuning

The PI gains of the inner current control are determined based on the filter impedance and desired time constant of the loop. The proportional (k_{pc}) and integral (k_{ic}) gains are defined as

$$k_{pc} = \frac{L_f}{\tau_s} \quad , \quad k_{ic} = \frac{R_f}{\tau_s} \qquad (20)$$

where L_f and R_f are the filter inductance and parasitic resistance, and τ_s is the desired time constant, typically in order of a few milliseconds. The PI controller of the outer AC voltage control loops can be defined as

$$k_{pv} = 2C_f D_v \omega_v \quad , \quad k_{iv} = \omega_v^2 C_f \qquad (21)$$

where D_v is the damping, commonly 0.707, and ω_v is the bandwidth of the voltage control loop, which is defined to be at least ten times slower than the inner current loops.

The tunings of the droop gains in the active and reactive power loops, k_p and k_q, respectively, are based on the maximum permissible deviations in the frequency and voltage,

$$k_p = 0.02 \, \omega_n/S_n \quad , \quad k_q = 0.1 \, V_n/S_n \qquad (22)$$

where ω_n, V_n, and S_n are the nominal frequency, voltage, and power of the VSC, respectively. Here, it is assumed that a

maximum of 2% of frequency and 10% of voltage deviations are allowed during transients.

The response time of the power-frequency droop in Mode 1 (grid-forming mode) is determined by the time constant of the low-pass filter, τ_p, and the droop gain, k_p. As discussed in [26], such response time is equivalent to the mechanical time constant that represents rotor inertia and calculated as

$$T_{vi} = \tau_p \, \frac{1}{k_p} \qquad (23)$$

where T_{vi} is the equivalent time constant, and k_p is expressed in per unit value (0.02 in this study). The response time of the grid-forming control (T_{vi}) should be slower than the response time of the electrolyzer (t_s) to make sure that the electrolyzer has enough time to respond to the power changes. Hence, the following constraint is assumed:

$$T_{vi} > t_s \qquad (24)$$

Based on (23) and (24), the cut-off frequency of the low-pass filter $G_p(s)$, which is given by (19), should satisfy the following requirement:

$$\tau_p > k_p t_s \qquad (25)$$

For the tunings of PI_v in Mode 2 and PI_p in Mode 3, a heuristic method is used. Since the outputs of all three operation modes are the frequency of HE VSC, they can be tuned to have a similar response time. Therefore, PI_v and PI_p are tuned to have a similar response time as in Mode 1.

D. Fault Operation

The HE VSC has to be protected during faults in the AC grid, as they may cause frequency deviation and overcurrent condition. To this aim, a rate limiter is placed on the frequency reference to limit the rate-of-change-of-frequency (ROCOF), and a qd-saturation block is placed on the current reference to protect the HE VSC from overcurrent conditions.
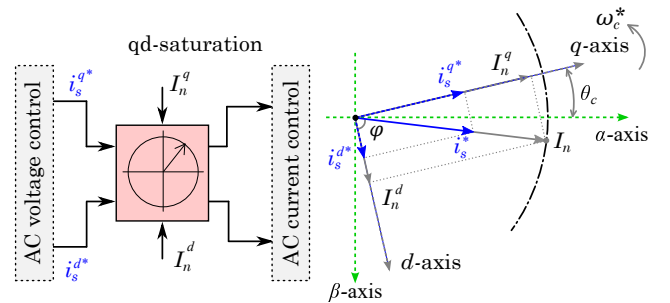

Fig. 4. Current saturation in qd-frame

During fault condition in the AC grid, the PCC voltage (v_c^{abc} in Fig. 1) dips to a low value. The PI controller of the AC voltage loop tries to bring the PCC voltage back to its nominal value by increasing the current reference. Note that the HE VSC does not inject any active current to the grid since it is a load by nature and it can only contribute reactive current. However, such reactive current contribution may exceed the converter's current rating. Hence, the qd-current saturation block is used to limit the magnitude of the VSC's current reference, i_s^{qd*}, while keeping its angle constant in qd-axis.

TABLE I
SYSTEM PARAMETERS

Parameter	Value
—Upstream AC Grid—	
Base RMS voltage, U_n	132 kV
Base power, S_n	50 MVA
Base frequency, f_n	50 Hz
—Power Transformer—	
short-circuit impedance	10%
HV/MV rated voltage	132/22 kV
—Voltage Source Converter—	
output L filter, L_f	5.09 mH
output C filter, C_f	67.66 μF
maximum current rating, I_n	1.2 pu
current loop PI controller	5.09+80/s
AC voltage loop PI controller	0.27+0.94/s
DC voltage loop PI controller	3.14e-04+1.57e-03/s
Active Power PI controller	1.25e-06+1.13e-05/s
power-frequency droop, k_p	0.02 pu
reactive power droop, k_q	0.1 pu
active power low-pass filter, $G_p(s)$	1/(1+0.04s)
reactive power low-pass filter, $G_q(s)$	1/(1+0.04s)
—DC/DC Converter—	
DC voltage loop PI controller	7.5e-05+7.5e-04/s
DC current loop PI controller	9.3e-04+2.4e-03/s
—PEM Electrolyzer—	
hydrogen tank capacity, V_H^*	9000 Moles
hydrogen production rate, m_H	10 Moles/MW/s
reverse reference voltage, V_{rev0}	400 V
double layer phenomenon, C_{op}	0.14 μF
double layer phenomenon, R_m	0.01 Ω
Faraday efficiency constants, α_1, α_2, α_3	96.5, 0.09, 75.5

The upper and lower saturation limits are set dynamically. Assuming the rated current of the VSC is I_n, and referring to Fig. 4,

$$I_n^q = I_n |\sin \phi| \ , \ I_n^d = I_n |\cos \phi| \qquad (26)$$

where ϕ is the angle of the current with respect to d-axis and simply calculated as $\phi = \arctan \frac{i_s^{q*}}{i_s^{d*}}$ The positive values of (26) define the upper limits of current, and the negative values set the lower limits. An anti-windup scheme is necessary to avoid integrator windup during current saturation. In this study, a conventional *back-calculation* anti-windup method is adopted [27].

IV. SIMULATION RESULTS

The performance of the PEM HE is tested in the power system shown in Fig. 5. Such test system is inspired from the Dalrymple substation located in Yorke Peninsula, Australia [28]; however, the original battery energy storage system at Dalrymple substation is replaced by the PEM HE and the total grid inertia and short-circuit ratio (SCR) are reduced to, respectively, 2 s and 3 in order to represent a low-inertia, weak network. The details related to the upstream AC grid are extracted from [29], [30].

The main parameters of the test system are given in Table (I). The VSC and DC-DC converter are simulated by their average models, and the DC-DC converter topology is based on the full-bridge structure. It is considered that the wind farm operates in GFL mode and tracks its maximum power point reference. The PEM HE is represented by its equivalent electrical circuit as shown in Fig. 3. It is assumed that the

response time of HE is 600 ms (please see Appendix) based on which the electrical elements of the equivalent model is calculated and given in Table (I). The rated capacity of the H$_2$ tank storage, V_H^*, is 9000 Moles. The hydrogen content in the tank is critically low if it hits the bottom 10% capacity ($V_H^{\min}$=0.1V_H^*), and the tank is full if it reaches to its 100% capacity ($V_H^{\max}$). The downstream dynamics of the hydrogen consumption is commonly very slow; hence, it is assumed that m_H' is constant in the next case studies. The following cases are considered:

- *Case study 1*: HE ability to flexibly adjust its power consumption, and therefore hydrogen production rate, in response to the variations in the wind power is studied. Also, the impact of power variations on the temperature and efficiency of HE stack is demonstrated.
- *Case study 2*: potential and limitations of three operation modes of HE (as discussed in Section III-B) in response to an under-frequency event in the upstream AC grid are investigated.
- *Case study 3*: HE ability to automatically switch among different operation modes, depending on its internal limitations and grid conditions is studied.
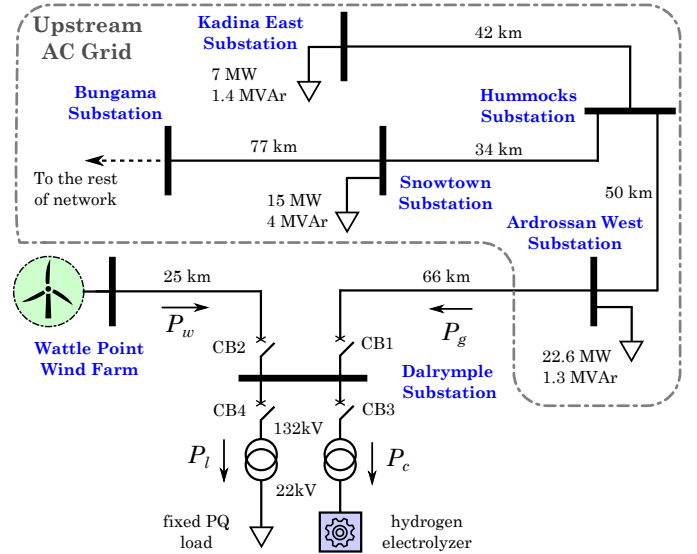- *Case study 4*: performances of HE and battery system while both operate in grid-forming mode are compared.

Fig. 5. Single line diagram of the test system

A. Case Study 1

In this case study, the power generated from the wind, P_w, varies with a ramp rate of 0.25 pu/s. It is first increased from 0.5 pu to 0.75 pu, then reduced again to 0.5 pu. After 2 s, it is further reduced to 0.25 pu. Finally, it is brought back to its initial operation point (0.5 pu). The constant PQ load has a fixed power consumption of P_l=0.23 pu, and the hydrogen consumption rate is fixed at m_H'=30 Moles/s for the entire period. First, it is considered that the HE is allowed to operate in Mode 1 (grid-forming mode) for the entire period, i.e., HE operates as a GFM load. It is assumed that the hydrogen production constraint as given by (16) is not violated and
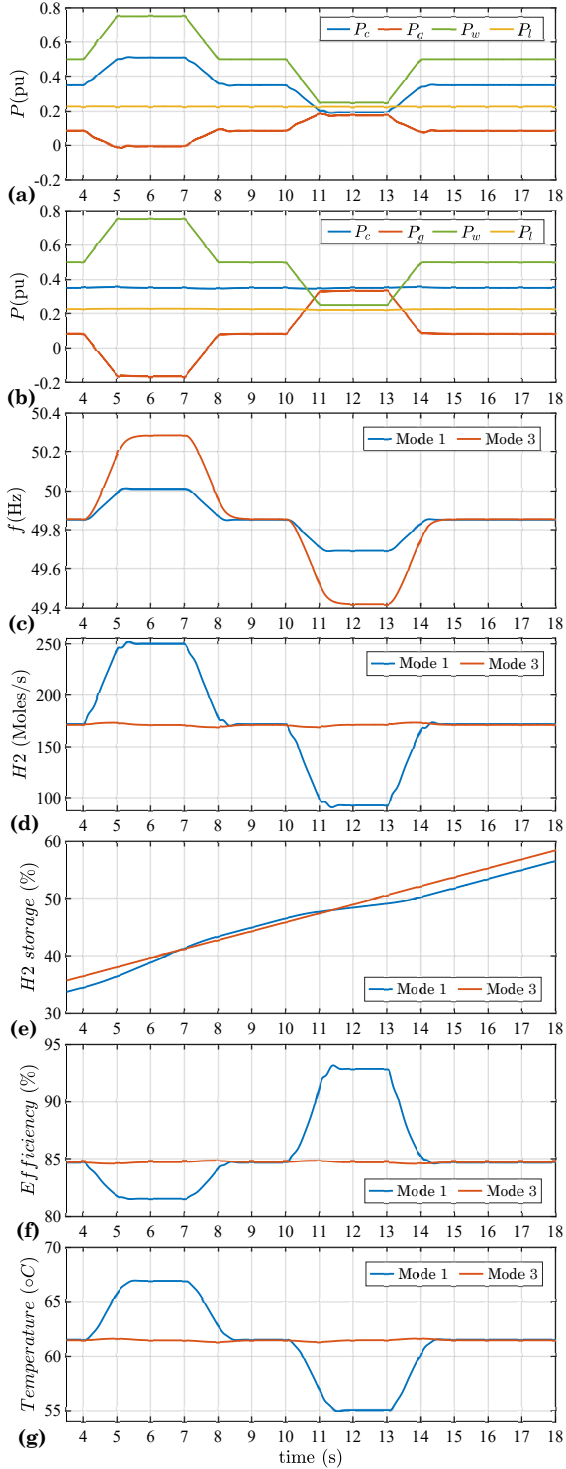
Fig. 6. HE's response to the wind power variations, (a) active powers for HE operating in Mode 1, (b) active powers for HE operating in Mode 3, (c) system frequency, (d) hydrogen production rate, (e) hydrogen content in the tank, (f) stack efficiency, and (g) stack temperature

the hydrogen content in the tank is within the limits. As illustrated in Fig. 6(a), the power consumption of the HE, P_c, flexibly follows the changes in the wind power based on the GFM law: it absorbs more power when there is higher power availability from the wind. Hence, the locally generated renewable power is consumed locally by the HE and fixed

load, and the upstream AC grid supplies the additional power (P_g). The changes in P_c reflects on the H$_2$ production rate, m_H, which is shown in Fig. 6(d). m_H varies from about 170 to nearly 250 Moles/s when the wind power reaches to its maximum value.

Opposite to this operation mode, the HE can operate as a constant power load, which is the operation Mode 3. This operation mode is activated in case that the lower limit on hydrogen content in the tank given by (16) is violated, so the HE operates in fixed power to fill the tank faster. Note that Mode 3 is activated manually in this case study only to compare performances of this operation mode with that of Mode 1. As shown in Fig. 6(b), regardless of the power availability from the wind or grid, the HE keeps consuming a constant power of 0.35 pu (operation Mode 3), and therefore, m_H is also constant at 170 Moles/s.

Comparing the frequency responses from the operation Mode 1 and 3, the power consumption flexibility provided by Mode 1 results in a smaller frequency deviation as shown in Fig. 6(c). This is resulted from the ability of HE to change its hydrogen consumption rate (m_H) quickly. However, such advantage is only secured if the capacity of H$_2$ storage is within the range [$V_H^{\min}$, $V_H^{\max}$], i.e., the storage is neither critically low, nor full. During this period, the level of hydrogen in storage reaches to about 60%, which is shown in Fig. 6(e).

The impacts of operation Mode 1 and 3 on the PEM stack's efficiency are compared in Fig. 6(f). As explained by (11), the stack's efficiency is a function of the stack's current. In operation Mode 1 (GFM mode), the stack's power varies based on the GFM control, leading to the variations in the stack current, which in turn changes the stack's efficiency (please also see Fig. 2). On the contrary, if the HE operates in Mode 3 (fixed power), the stack's current, and therefore stack efficiency, remains constant during operation as long as the power set-point is not changed. Similar situation exists for the stack's temperature. For the operation Mode 1, the stack's temperature varies according to the changes in the stack's power. Higher power consumption increases stack's temperature since part of this power (depending on the stack's efficiency) is dissipated as heat inside the stack. The stack's temperature is constant in operation Mode 3 as illustrated in Fig. 6(g).

This case study thus indicates that a HE which operates in GFM mode can provide frequency regulation and flexibly adjust its power consumption according to the availability of power generation in the network. However, such HE operation may require further control and arrangement to keep HE's temperature and efficiency within an acceptable range.

B. Case Study 2

In this case study, an under-frequency event occurs in the upstream AC grid at t=4 s. The dynamic behaviour of HE in the proposed operation modes is discussed. If the HE operates in Mode 1 (grid-forming control) prior to the under-frequency event, it reduces its power consumption to avoid large frequency deviation as shown in Fig. 7. P_c is reduced (based on droop fucntion) from 0.5 pu to 0.24 pu, so more power from
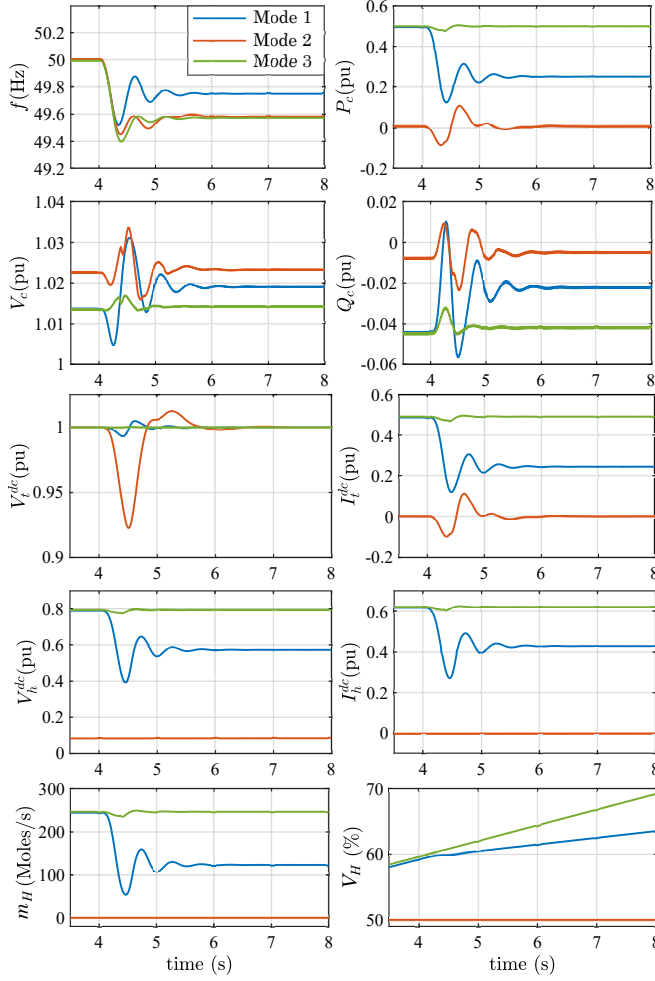
Fig. 7. HE's response to an under frequency event in the upstream AC grid, comparing performances of Mode 1, Mode 2, and Mode 3

the wind is injected to the grid, helping with the frequency recovery. Accordingly, m_H reduces from 250 to 120 Moles/s. Operation Mode 3 (constant power control) is indifferent to the under-frequency event, and keeps consuming P_c=0.5 pu for the production of m_H=250 Moles/s. The frequency deviation is larger in this mode.

Different from Mode 1 and 3, in the operation Mode 2 (DC voltage control), the HE is shut down (m_H=0 Moles/s) and disconnected (due to internal fault) prior to the event. Only the HE VSC remains connected to the grid for the AC voltage regulations. Such operation mode cannot help with the frequency response as the HE power consumption is zero.

Regardless of the operation modes, DC-link voltage, V_t^{dc}, and AC voltage, V_c, remained regulated within the permissible range as it can be seen from Fig. 7. The current flowing into the HE, I_h^{dc}, is zero during operation Mode 2 since the HE is shut down and disconnected, and V_h^{dc} remains at the open-circuit voltage level. The initial hydrogen content in the tank is V_H^0=50% at t=0 s. While it remains unchanged during operation Mode 2, it increases during operation Mode 1 and 3 with different rates.
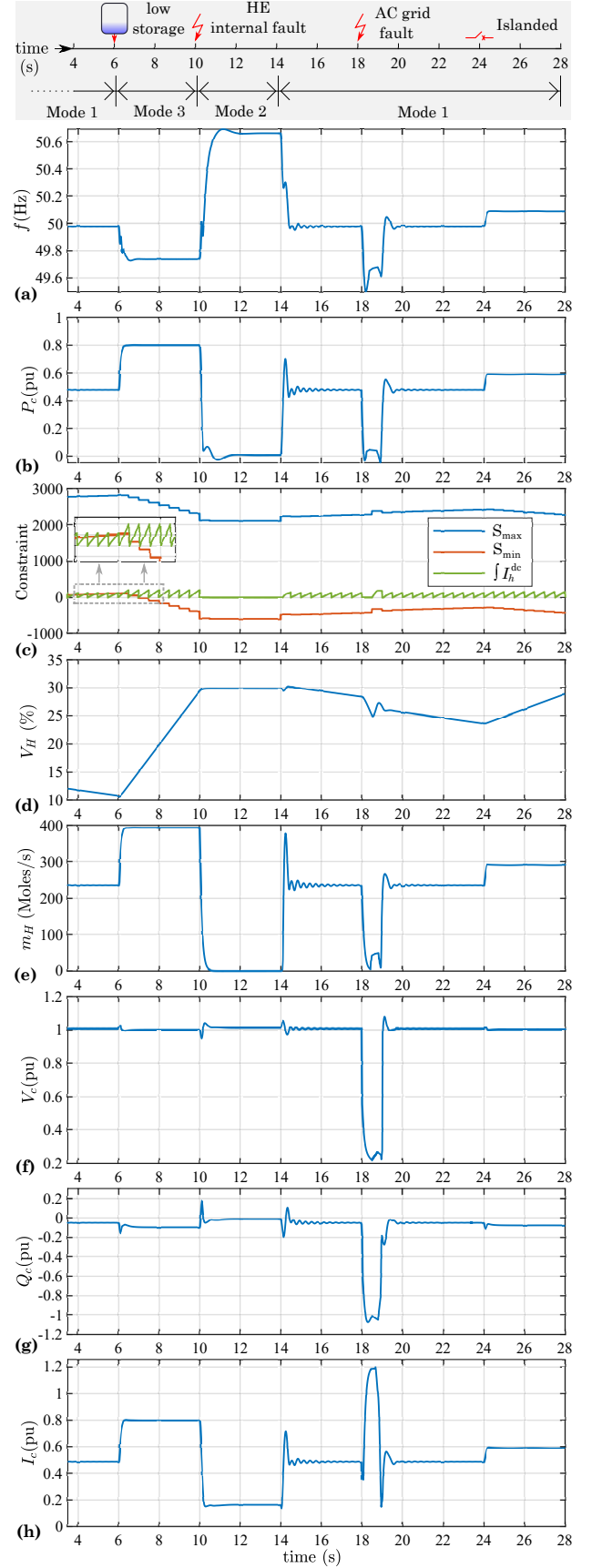

Fig. 8. Transient responses of HE while switching among different modes during various internal and external events, (a) frequency, (b) active power, (c) hydrogen constraint, (d) hydrogen content, (e) hydrogen production rate, (f) AC voltage, (g) reactive power, and (h) stack current

C. Case Study 3

In this case study, the HE ability to transiently switch among different operation modes, depending on its internal limitations and grid operation, is explored. The operation modes (1,2, and 3) are automatically selected by calculating the hydrogen production constraint given by (16) in real time. The timeline of the events is shown on the top of Fig. 8. Initially, the HE operates in Mode 1 (GFM mode), and the initial hydrogen content in the tank is only 13%. The hydrogen consumption rate (m'_H=250 Moles/s) is higher than its production rate (m_H=230 Moles/s), so the hydrogen in the tank is reduced over time. The condition that the HE is allowed to operate in Mode 1 is explained by (16), which is plotted in Fig. 8(c). The green curve is the integral of I_h^{dc} for the time horizon of 0.5 s. After each time horizon, the integrator is reset. At t=6 s, $S_{\min}$ (red line) hits the peak of the green line, meaning that the operation Mode 1 is no longer feasible since the storage is critically low. Hence, the operation mode of HE is automatically switched to Mode 3 in order to increase the power consumption of the HE, and therefore, store hydrogen at a higher rate (m_H=400 Moles/s) to fill the storage faster (see Fig. 8(e)).

After few seconds, an internal fault occurs inside the HE at t=10 s, causing the plant to shut down. However, the VSC remains at the service by switching its operation mode to Mode 2. Since the plant is shut down, m_H=m'_H=0. The HE VSC only regulates V_t^{dc} and V_c during this period.

The internal fault is cleared and the HE is back to operation after 2 seconds. Once the HE is back online, and $S_{\min}$ and $S_{\max}$ are not violated, it switches to operation Mode 1 again. Subsequently, a three-phase fault occurs in the Dalrymple substation at t=18 s and cleared after 800 ms. During fault period, voltage dips to about 0.2 pu causing the power consumption of HE to drop to zero. However, the HE VSC remains connected to the faulty substation to provide voltage support by injecting reactive power, Q_c. As it can be seen from Fig. 8(h), the HE VSC's full current capacity (1.2 pu) is used for reactive power injection. The fault performance shown in this case study is related to operation Mode 1. It is to note that the fault performance of HE depends on its operation mode. In particular, the post-fault performance of operation Mode 2 and Mode 3 differs from that of Mode 1 since they have different outer control structures. Finally, a system separation occurs at t=24 s, and the upstream grid is disconnected (CB1 is open). The islanded system consisting of the HE, wind energy, and the fixed load, continues stable operation since the HE, operating in GFM mode, is forming the voltage and frequency of the islanded system.

The GFM HE (operation Mode 1) adjusts its power consumption to reduce the frequency deviation in the network. Thus, the power consumption of the HE depends on the power imbalance in the upstream grid. The secondary controller shown in Fig. 1 can ensure that the HE power consumption goes slowly back to a default value (P^{ref}) after the primary frequency response. It is to note that P_c^* is the power reference for droop control, while P^{ref} is a power reference to a slow PI controller which is located in the secondary control.
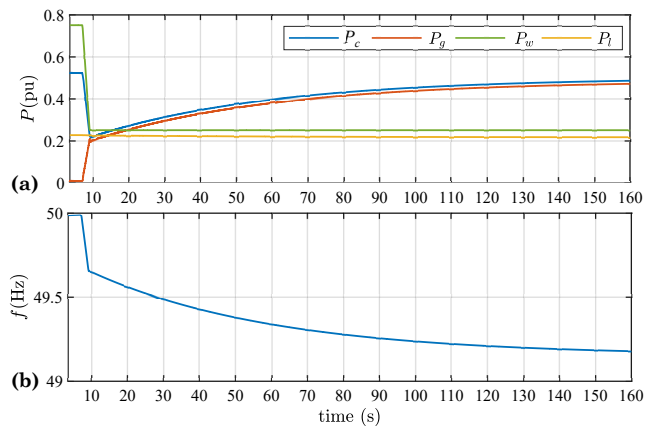

Fig. 9. Impact of secondary controller on the HE GFM operation, (a) active power, and (b) frequency

Considering the case study 3 and assuming that the wind power reduces from 0.75 pu at t=7 s to 0.25 pu with a ramp rate of 0.25 pu/s, the impact of the slow secondary controller on the HE GFM operation is shown in Fig. 9. The GFM HE primary response (first few seconds) depends on the droop control, while the steady-state operation (with a settling time of few minutes) relies on the secondary controller. Here it is assumed that P^{ref} and P_c^* are equal; however, they can be different. The activation of secondary controller can ensure a default steady-state power consumption (P^{ref}) can be reached after disturbances, but at the cost of a larger steady-state frequency deviation (see Fig. 9(b)). If the secondary controller is deactivated, the steady-state power consumption of HE differs from P^{ref} and depends on the power imbalance in the grid, which results in a smaller frequency deviation. The deactivation of the secondary controller is more consistent with the grid-forming functionality as it results in smaller frequency deviation; however, both options are available in the suggested control scheme for selection.

This case study illustrates a great HE potential in providing grid-forming services to the network even during islanded operation. Therefore, PEM HE can be considered as a potential rival for other technologies capable of offering grid-forming provisions (e.g., synchronous machine).

D. Case Study 4

The Dalrymple substation originally has a battery storage system which has been replaced by the HE in the previous case studies. In this final case study, a comparison between PEM HE and a battery storage system in terms of their capability in providing grid-forming services is presented.

Two scenarios are briefly studied. In the first scenario, the previous test system with the electrolyzer is considered where constant PQ load consumes P_l=0.35 pu and the wind power gradually reduces from P_w=0.8 pu to 0.4 pu with a ramp rate of 0.2 pu/s. At t=6 s, the upstream grid is disconnected, and electrolyzer continues to form the grid (operation Mode 1). During the period of 8 to 14 s, the generated power from the wind is not sufficient to meet the load demand (constant PQ load and electrolyzer); hence, the electrolyzer automatically reduces its power consumption to obtain the required power
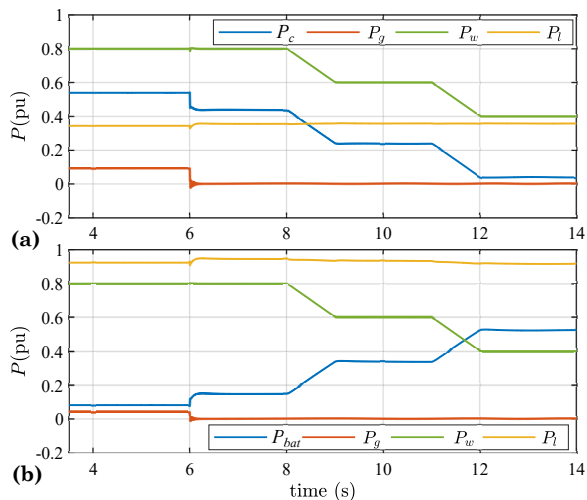
Fig. 10. Comparison between performances of electrolyzer and battery system, (a) system with electrolyzer, and (b) system with battery system

Fig. 11. Test system simulated in real-time

Fig. 12. Control hardware-in-the-loop setup

balance in the system as shown in Fig. 10(a). Therefore, the required grid-forming services are supplied from the load side (electrolyzer).

In the second scenario, the electrolyzer is replaced by a battery system of similar size. The constant load consumes P_l=0.92 pu and the wind power follows similar pattern as the previous scenario. As it can be seen from Fig. 10(b), the wind power is not sufficient to supply the constant PQ load; therefore, the power generation of battery system, P_{bat}, gradually increases to compensate the reduction in the wind power. Hence, the required grid-forming capability is on the source side (battery system).

From the simulation results, it can be concluded that both electrolyzer and battery system can provide grid-forming services to the grid, even after system separation. Hence, in terms of grid-forming functionality, both technologies have fast response and are capable of providing such services. However, hydrogen has many uses in transportation and industry sectors in addition to be a great power-to-gas energy storage solution.

V. CONTROL HARDWARE-IN-THE-LOOP TESTS

In order to verify the robustness and effectiveness of the proposed concept, the HE control system is embedded and tested in hardware running in real-time. The algorithm is embedded in a Texas Instruments Microcontroller Unit (MCU) F28335 evaluation board and the power grid is simulated in real-time in a Typhoon HIL 602+ device. The digital control algorithm samples signals at the rate of 20 kHz. The system simulated in real-time is shown in Fig. 11. It is composed of a PEM hydrogen electrolyzer with the proposed control system and an equivalent representation of the upstream AC grid with dynamics given by a simplified turbine and governor [31]. The governor model is based on a droop gain as given by $k_{droop} = 15.7$, and the turbine dynamic is simulated by the transfer function $T_r(s)=k_{hp} + \frac{k_{lp}}{\tau_{rh}s+1}$ whose parameters are $k_{hp} = 0.3$, $k_{lp} = 0.7$, $\tau_{rh} = 0.1$ s. The equivalent inertia and SCR of the grid are 2 s, and 3, respectively. The converter nominal voltage and power are 22 kV and 50 MVA, respectively.
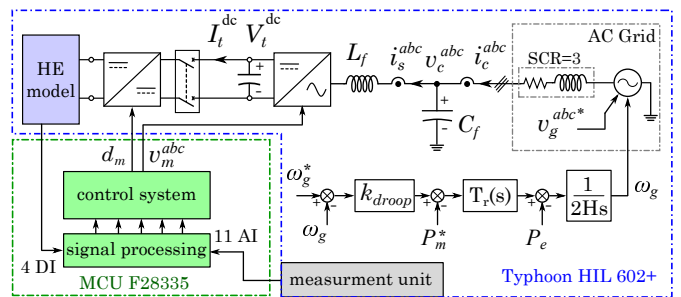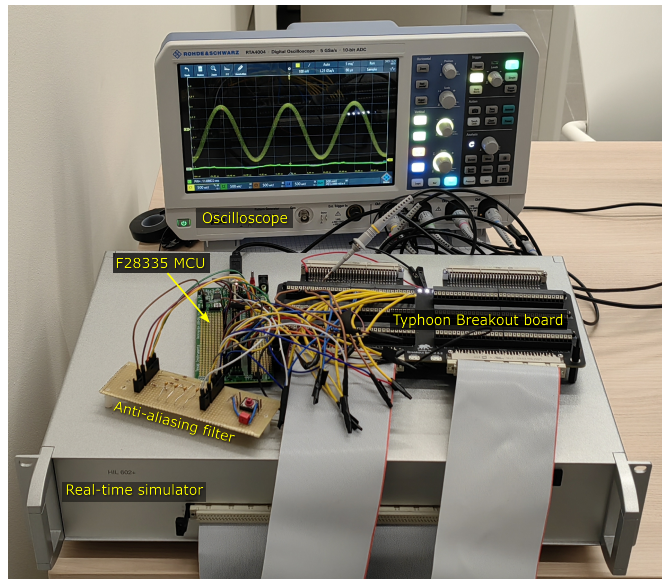
A. Experimental setup

The experimental setup is shown in Fig. 12. Eleven analog signals (AI), including $v_c^{abc}, i_c^{abc}, i_s^{abc}, V_t^{dc}$ and I_t^{dc} as indicated in Fig. 1, and four digital signals (DI) related to the operating mode selection (OP_1, OP_2, OP_3 and $Enable$) are sent by the Typhoon HIL to the MCU. The analog signals are scaled between 0–3 V before sending to the MCU. The first three digital signals indicate the three operation modes as explained in Section III-B, and the last digital signal enables the controller. The MCU outputs are the three-phase voltage of converter, v_m^{abc}, and d_m, as highlighted in Fig. 1. The output three-phase signals are modulated by a PWM at 10 kHz and filtered by the passive first-order anti-aliasing filters before sending them back to Typhoon HIL. The filter parameters are: $R = 1000\ \Omega$, $C = 0.1\ \mu$F with a cut-off frequency of 1591 Hz.

B. Experimental results

Two test cases are discussed. The purpose of the first test case is to confirm the ability of the proposed HE controller to dynamically switch among three operation modes in real-time. As it is presented in Fig. 13, the HE operates in Mode 1 in the period of 0 to 1.5 s. Subsequently, HE switches to operation Mode 3 and 2 at 1.5 s and 3 s, respectively. The operation modes are communicated between MCU and real-time simulator via OP digital signals. Referring to Fig. 13, it
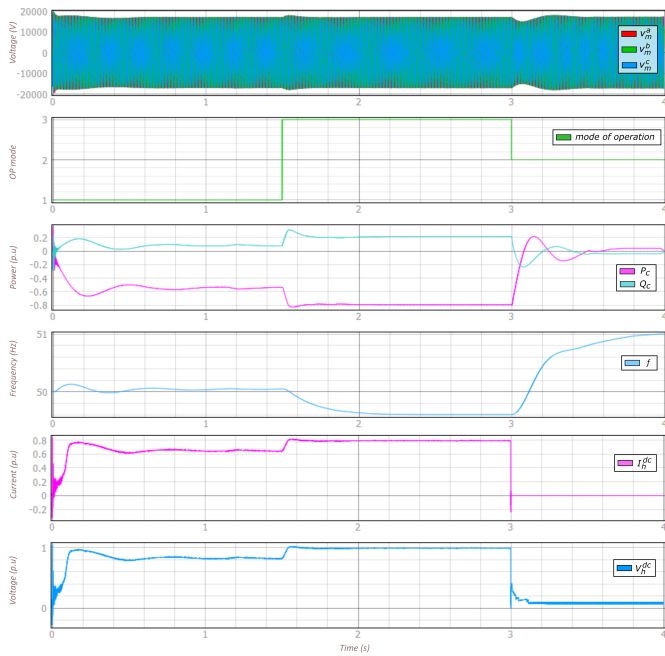
Fig. 13. Test case 1: (a) v_m^{abc} output from the MCU, (b) operation modes sent to the MCU, (c) HE active and reactive power, (d) system frequency, (e) HE current, and (f) HE DC voltage
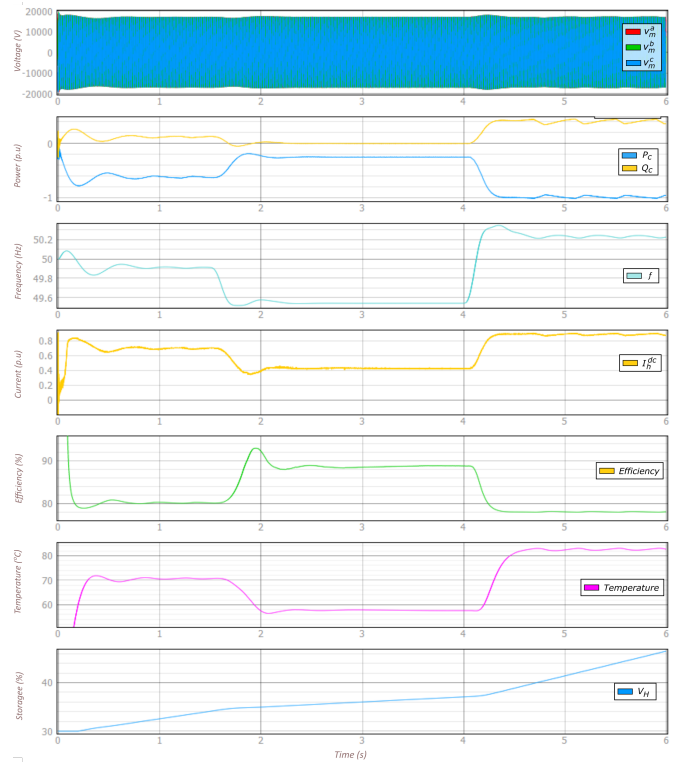

Fig. 14. Test case 2: (a) v_m^{abc} output from the MCU, (b) HE active and reactive power, (c) system frequency, (d) HE current, (e) HE efficiency, (f) HE temperature, and (g) hydrogen content in the tank

can be observed that the transition among different operation modes are preformed smoothly and without a major transient or unwanted dynamics, which is consistent with the results obtained from simulation.

The second test case focuses on the HE performance in operation Mode 1 (GFM mode) during frequency events in the upstream grid. An under-frequency event occurs at t=1.5 s which is followed by an over-frequency event at t=4 s. As it is shown in Fig. 14, the HE reacts to those frequency events by decreasing and increasing its power consumption, respectively. The over-frequency event causes an increase of 0.75 Hz in the system frequency. The HE immediately increases its power consumption in an attempt to reduce frequency deviation. However, the HE power consumption reaches to about 1 pu that is the maximum frequency support that the HE can provide for the grid. During this frequency excursion, the stack temperature and efficiency also vary as shown in Fig. 14. Although different systems have been analyzed in simulation and in real-time, the results in real-time confirm that the HE can successfully operate in GFM mode and switch stably among all operation modes. Such stable operation and smooth transition among modes can be observed from Fig. 13 and Fig. 14.

VI. CONCLUSION

This study proposed a control system for a PEM hydrogen electrolyzer, which consists of three operation modes: grid-forming mode (Mode 1), DC voltage mode (Mode 2), and constant power mode (Mode 3). The activation of each operation mode was carried out automatically based on the hydrogen production constraint. The operation Mode 1 (grid-forming) was selected if the upper and lower limits given by the hydrogen production constraint were not violated, i.e.,

there is sufficient headroom/footroom in hydrogen storage tank. So, the electrolyzer could fully participate in forming the voltage and frequency of the grid. If the upper limit of the constraint was violated (i.e., the hydrogen tank was nearly full) or an internal failure has occurred in the electrolyzer, operation Mode 2 was activated. In this mode, the electrolyzer has to be shut down for safety, but its VSC could remain connected to the AC grid to provide voltage regulation services. In case the lower limit of the constraint was violated (i.e., the hydrogen content in the tank was critically low), the operation Mode 3 was activated. In this mode, the VSC was operating in constant power mode and extracting maximum power from the grid to quickly fill the hydrogen tank in order to avoid interruption in hydrogen supply for the downstream process. The PEM electrolyzer with the proposed control system has been tested on a low-inertia grid whose topology is inspired by a portion of the transmission grid in South Australia. The following points can be concluded from the simulation results: (i) an electrolyzer has a great potential to provide grid-forming services (frequency and voltage regulations) to the network, (ii) with the tandem operation with a nearby wind generation system, a grid-forming electrolyzer can form the voltage and frequency of an islanded network, (iii) the grid-forming operation of an electrolyzer is only allowed if the hydrogen production constraints are not violated; in case of violation, the operation mode of electrolyzer should switch to either DC voltage mode or constant power mode depending on the hydrogen production conditions, and (vi) electrolyzer can have the same grid-forming capability as a battery storage
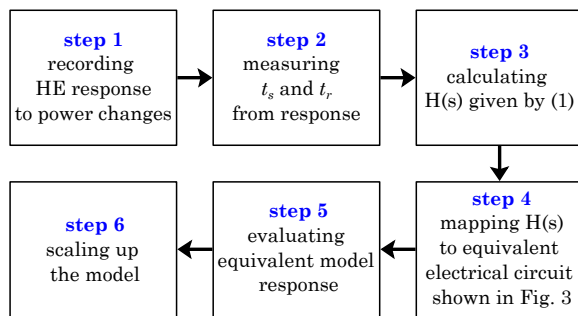
Fig. 15. Steps for HE equivalent model validation

Fig. 16. Response evaluation of the HE equivalent model

system. The difference is that such services can come from the load side (electrolyzer), or source side (battery system). The results from the tests in hardware confirm that the proposed concept can be successfully implemented in practice.

APPENDIX
ELECTROLYZER MODEL VALIDATION

In order to evaluate the accuracy of the HE equivalent electrical model which is shown in Fig. 3, its response is compared with the experimental results obtained in [2]. The steps that are followed for the HE equivalent model validation are shown in Fig. 15. In the step 1, the power consumption of HE is varied and the DC current is recorded [2]. The tests are conducted on a 40 kW PEM electrolyzer, so the equivalent model is validated for this rated power but later it is scaled up for a MW-scale PEM HE that is used in the case studies. As discussed in Section II.C, only the rise time (t_r) and settling time (t_s) are needed to identify the model of a HE. Such information is extracted from the responses in the step 2. Please note that the HE has a first-order response to power variations [2], [23]. Having t_r and t_s, the transfer function $H(s)$, given by (1), is calculated in the step 3. Next, $H(s)$ is mapped to an equivalent electrical circuit (shown in Fig. 3) in the step 4. In the step 5, the similar tests as in [2] are carried out on the HE equivalent circuit to validate the accuracy of the model. Once the equivalent model is validated for a 40 kW electrolyzer, the model is scaled up for the high-power HE used in this study.

The experimental results on a 40 kW PEM HE are compared with the results obtained from the equivalent electrical circuit in Fig. 16. The trigger signal is used to change the DC power consumption of HE. The power consumption is changed (i) from 25% to 100%, (ii) from 50% to 100%, and (iii) from 75% to 100%, and the DC current of HE is plotted for every cases. As it can be seen, the responses of the equivalent electrical circuit and the experimental results have a good matching. The DC current reaches to its reference value after about 150 ms in all cases. However, this evaluation is valid for a 40 kW HE while we use MW-scale HE in our study. Hence, we need to scale-up the equivalent circuit to have realistic response for a MW-scale electrolyzer.

Here we need to make some assumptions. Referring to [32], a MW-scale HE consists of arrays of HE modules. Each HE module can have the nominal power of 150-250 kW. Then, such modules are connected in a form of an array to scale
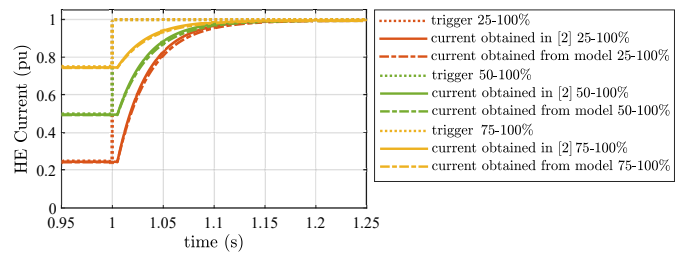
up HE's power. From the test results on a 40 kW HE, we can conclude that the HE can vary its power consumption from 0 to 40 kW within 150 ms. So, we may assume that each HE module of 150-250 kW is able to change its power consumption from 0 to the rated value within the range of 400-700 ms. In this study, we use 600 ms as the settling time of each HE module.

Since a MW-scale HE is built by an array of HE modules, we assume here that the HE modules have similar DC rated voltage and they are connected in parallel to the main DC bus. Hence, the settling time of each module (600 ms) is in fact the settling time of the entire HE arrays. By such assumptions, we re-calculate the HE transfer function, $H(s)$, based on the new settling time (600 ms) and map it to the equivalent electrical circuit. Please note that the response time of the HE is an input parameter to the equivalent model calculation. So, any response time, which could be faster or slower than 600 ms, can be used to derive the equivalent model.

REFERENCES

[1] IRENA, "Green hydrogen cost reduction," 2020. [Online]. Available: https://www.irena.org/-/media/Files/IRENA/Agency/Publication/2020/Dec/IRENA_Green_-hydrogen_cost_2020.pdf

[2] J. Eichman, K. Harrison, and M. Peters, "Novel electrolyzer applications: Providing more than just hydrogen," NREL, Tech. Rep., 9 2014. [Online]. Available: https://www.osti.gov/biblio/1159377

[3] Gigastack, "Bulk supply of renewable hydrogen," Element Energy, Tech. Rep., February 2020. [Online]. Available: https://gigastack.co.uk/content/uploads/2020/06/Gigastack-Phase-1-Public-Summary.pdf

[4] J. J. Caparrós Mancera, F. Segura Manzano, J. M. Andújar, F. J. Vivas, and A. J. Calderón, "An optimized balance of plant for a medium-size pem electrolyzer: Design, control and physical implementation," *Electronics*, vol. 9, no. 5, 2020.

[5] T. H. Ruggles, J. A. Dowling, N. S. Lewis, and K. Caldeira, "Opportunities for flexible electricity loads such as hydrogen production from curtailed generation," *Advances in Applied Energy*, vol. 3, p. 100051, 2021.

[6] N. Gyawali and Y. Ohsawa, "Integrating fuel cell/electrolyzer/ultracapacitor system into a stand-alone microhydro plant," *IEEE Transactions on Energy Conversion*, vol. 25, no. 4, pp. 1092–1101, 2010.

[7] M. Korpas and A. Holen, "Operation planning of hydrogen storage connected to wind power operating in a power market," *IEEE Transactions on Energy Conversion*, vol. 21, no. 3, pp. 742–749, 2006.

[8] A. M. O. Haruni, M. Negnevitsky, M. E. Haque, and A. Gargoom, "A novel operation and control strategy for a standalone hybrid renewable power system," *IEEE Transactions on Sustainable Energy*, vol. 4, no. 2, pp. 402–413, 2013.

[9] J. Li, J. Lin, H. Zhang, Y. Song, G. Chen, L. Ding, and D. Liang, "Optimal investment of electrolyzers and seasonal storages in hydrogen supply chains incorporated with renewable electric networks," *IEEE Transactions on Sustainable Energy*, vol. 11, no. 3, pp. 1773–1784, 2020.

[10] A. M. Abomazid, N. El-Taweel, and H. E. Farag, "Optimal energy management of hydrogen energy facility using integrated battery energy storage and solar photovoltaic systems," *IEEE Transactions on Sustainable Energy*, pp. 1–1, 2022.

[11] A. E. Samani, A. D'Amicis, J. D. De Kooning, D. Bozalakov, P. Silva, and L. Vandevelde, "Grid balancing with a large-scale electrolyser providing primary reserve," *IET Renewable Power Generation*, vol. 14, no. 16, pp. 3070–3078, 2020.

[12] N. Veerakumar, Z. Ahmad, M. E. Adabi, J. R. Torres, P. Palensky, M. van der Meijden, and F. Gonzalez-Longatt, "Fast active power-frequency support methods by large scale electrolyzers for multi-energy systems," in *2020 IEEE PES Innovative Smart Grid Technologies Europe (ISGT-Europe)*, 2020, pp. 151–155.

[13] M. Ghazavi Dozein, A. Maria De Corato, and P. Mancarella, "Fast frequency response provision from large-scale hydrogen electrolyzers considering stack voltage-current nonlinearity," in *2021 IEEE Madrid PowerTech*, 2021, pp. 1–6.

[14] M. G. Dozein, A. Jalali, and P. Mancarella, "Fast frequency response from utility-scale hydrogen electrolyzers," *IEEE Transactions on Sustainable Energy*, vol. 12, no. 3, pp. 1707–1717, 2021.

[15] O. Gomis-Bellmunt, S. Dadjo Tavakoli, V. Lacerda, and E. Prieto-Araujo, "Grid-forming loads: Can the loads be in charge of forming the grid in modern power systems?" *under revision in IEEE Transactions on Smart Grid*, pp. 1–12, 2022.

[16] X. Quan, Q. Hu, X. Dou, Z. Wu, L. Zhu, and W. Li, "Control of grid-forming application for fuel cell/electrolyser system," *IET Renewable Power Generation*, vol. 14, no. 17, pp. 3368–3374, 2020. [Online]. Available: https://ietresearch.onlinelibrary.wiley.com/doi/abs/10.1049/iet-rpg.2020.0508

[17] K. Prabakar, Y. Nag Velaga, R. Flores, J. Brouwer, J. Chase, and P. Sen, "Enhancing distribution system resiliency using grid-forming fuel cell inverter," NREL, Tech. Rep., 2022. [Online]. Available: https://www.nrel.gov/docs/fy22osti/82111.pdf

[18] P. Lettenmeier, "Efficiency – electrolysis," Siemens, Tech. Rep., 2020. [Online]. Available: https://assets.siemens-energy.com/siemens/assets/api/uuid:5342163d-2333-4c8d-ae85-2a0e8d45db56/white-paper-efficiency-en.pdf

[19] T. Yigit and O. F. Selamet, "Mathematical modeling and dynamic simulink simulation of high-pressure pem electrolyzer system," *International Journal of Hydrogen Energy*, vol. 41, no. 32, pp. 13 901–13 914, 2016.

[20] N. Cooper, C. Horend, F. Röben, A. Bardow, and N. Shah, "A framework for the design & operation of a large-scale wind-powered hydrogen electrolyzer hub," *International Journal of Hydrogen Energy*, vol. 47, no. 14, pp. 8671–8686, 2022. [Online]. Available: https://www.sciencedirect.com/science/article/pii/S0360319921050278

[21] B. Han, S. M. Steen, J. Mo, and F.-Y. Zhang, "Electrochemical performance modeling of a proton exchange membrane electrolyzer cell for hydrogen energy," *International Journal of Hydrogen Energy*, vol. 40, no. 22, pp. 7006–7016, 2015. [Online]. Available: https://www.sciencedirect.com/science/article/pii/S036031991500837X

[22] B. Flamm, C. Peter, F. N. Büchi, and J. Lygeros, "Electrolyzer modeling and real-time control for optimized production of hydrogen gas," *Applied Energy*, vol. 281, p. 116031, 2021.

[23] M. G. Dozein, A. M. De Corato, and P. Mancarella, "Virtual inertia response and frequency control ancillary services from hydrogen electrolyzers," *IEEE Transactions on Power Systems*, pp. 1–12, 2022.

[24] M. Castañeda, A. Cano, F. Jurado, H. Sánchez, and L. M. Fernández, "Sizing optimization, dynamic modeling and energy management strategies of a stand-alone pv/hydrogen/battery-based hybrid system," *International Journal of Hydrogen Energy*, vol. 38, no. 10, pp. 3830–3845, 2013.

[25] Y. Khayat, Q. Shafiee, R. Heydari, M. Naderi, T. Dragičević, J. W. Simpson-Porco, F. Dörfler, M. Fathi, F. Blaabjerg, J. M. Guerrero, and H. Bevrani, "On the secondary control architectures of ac microgrids: An overview," *IEEE Transactions on Power Electronics*, vol. 35, no. 6, pp. 6482–6500, 2020.

[26] S. D'Arco and J. A. Suul, "Equivalence of virtual synchronous machines and frequency-droops for converter-based microgrids," *IEEE Trans. Smart Grid*, vol. 5, no. 1, pp. 394–395, 2014.

[27] S. Dadjo Tavakoli, E. Prieto-Araujo, O. Gomis-Bellmunt, and S. Galceran-Arellano, "Fault ride-through control based on voltage prioritization for grid-forming converters," *IET Renewable Power Generation*, vol. n/a, no. n/a, 2023. [Online]. Available: https://ietresearch.onlinelibrary.wiley.com/doi/abs/10.1049/rpg2.12682

[28] Electranet, "Dalrymple escri-sa battery project," 2022. [Online]. Available: https://www.electranet.com.au/electranets-battery-storage-project

[29] AEMO, "Australian electricity network map," 2022. [Online]. Available: https://www.aemo.com.au/aemo/apps/visualisations/map.html

[30] SA Power Network, "Zone substation data," 2020. [Online]. Available: https://www.sapowernetworks.com.au/data/308954/2019-2020-zone-substation-data

[31] P. Kundur, *Power System Stability and Control*. CRC Press, may 2007.

[32] K. Harrison, "Mw-scale pem-based electrolyzers for res applications," NREL, Tech. Rep., 2021. [Online]. Available: https://www.nrel.gov/docs/fy20osti/79055.pdf